

Atelosite-(Y), a new rare earth defect silicate of the KDP structure type

THOMAS MALCHEREK^{1,*}, BORIANA MIHAILOVA¹, JOCHEN SCHLÜTER¹ and TOMAS HUSDAL²

¹ Mineralogisch-Petrographisches Institut, Universität Hamburg, Grindelallee 48, 20146 Hamburg, Germany

*Corresponding author, e-mail: thomas.malcherek@uni-hamburg.de

² Veslefrikk 4, 8028 Bodø, Norway

Abstract: The title mineral has been discovered in a granitic pegmatite at the Stetind quarry, Tysfjord, Norway. Atelosite-(Y) forms pale brown to colourless, transparent crystals of dipyramidally terminated, short-prismatic habit with a diameter of up to 0.3 mm. Based on electron microprobe analysis and 16 anions per formula unit, the empirical formula is $(Y_{3.11}Yb_{0.46}Er_{0.19}Dy_{0.11}Gd_{0.09}Ho_{0.01}Tb_{0.02})_{\Sigma 3.99}Si_{2.40}O_{16}H_{10.43}$. The presence of hydroxyl-groups is inferred from the detection of OH-stretching modes near 3225 cm^{-1} in Raman spectra of the new mineral. The crystal structure of atelosite was solved and refined on single-crystal X-ray diffraction data in space group $I42d$, with $a = 6.947(4)$, $c = 6.133(3)$ Å, $V = 295.98(28)$ Å³. Site occupancy refinement at the 4a-site approaches 3/4 Si-occupancy, if the 4b-site is fully occupied by Y and Yb, with a refined Y/Yb ratio of 4. This suggests an idealized formula of $Y_4Si_3O_8(OH)_8$ for atelosite-(Y). The crystal structure of the new mineral is of particular interest with regard to the known occurrence of hydrous species in the nominally anhydrous minerals xenotime and zircon.

Key-words: rare earth elements, zircon, xenotime mineral, atelosite-(Y), new mineral, crystal structure, yttrium silicate hydrate, tetrahedral vacancy, KDP structure type, Stetind (Tysfjord, Norway).

1. Introduction

The defect related occurrence of hydrous species in the nominally anhydrous mineral zircon, $ZrSiO_4$, is a well documented phenomenon (Woodhead *et al.*, 1991; Nasdala *et al.*, 2001; Trail *et al.*, 2011). Experimental observation of these hydrous species has been mainly carried out by spectroscopic methods, with different models accounting for the occurrence of various observed O-H stretching absorption bands (Nasdala *et al.*, 2001). According to one of these models, the presence of hydrogen in zircon is not associated with cation vacancies in its immediate neighbourhood, but possibly with substitution of trivalent cations for Zr^{4+} . The corresponding O-H bonds are almost parallel to $\langle 100 \rangle$, giving rise to an infrared absorption band at 3385 cm^{-1} . The other two models suggested by the same authors assume that the structural incorporation of hydrogen is coupled either to Zr or to Si vacancies, which results in the formation of OH groups perpendicular or parallel to $[001]$, generating infrared absorption bands near 3180 and 3420 cm^{-1} , respectively. Similarly, defect related OH-groups have been reported for the isostructural xenotime, $(Y,Yb)PO_4$ (Talla *et al.*, 2011). To the authors knowledge only minor amounts of hydrous species in well crystallized xenotime and zircon have been reported so far, while the water-rich end-member compositions of the postulated substitution schemes are not known.

The Tysfjord granite with its niobium-yttrium-fluorine (NYF) type pegmatites is a well-known source for rare minerals in Norway. Close to 150 different species have

been identified from these pegmatites (Husdal, 2008), of which 43 are rare earth element (REE) minerals, mainly formed in association with Y-bearing fluorite. This fluorite was described as a new mineral under the name “yttrofluorite” by Vogt (1911), but was later discredited. Three new species have so far been discovered in these assemblages: hundholmenite-(Y) (Raade *et al.*, 2007), stetindite (Schlüter *et al.*, 2009) and fluorbritholite-(Y) (Pekov *et al.*, 2011). Particularly the Stetind pegmatite, exposed by quarrying in 1961 and 1962, contains fluorite with numerous inclusions of different REE-minerals. During the summer of 2008, one of us (TAH) collected a sample on the dumps of the Stetind pegmatite, containing an unknown, tetragonal Y-silicate. We here describe this new mineral, named atelosite-(Y) from Greek atels ($\alpha\tau\epsilon\lambda\eta\varsigma$) meaning deficient, based on the Si-deficiency of the mineral. Both the mineral and the name were approved by the IMA-CNMNC (IMA 2010-065). The holotype is preserved in the collection of the Mineralogical Museum of the University of Hamburg, Germany, under catalogue number NO-004. Further information on the type material will be available at the Type Specimen Catalogue Germany (www.typmineral.uni-hamburg.de).

2. Experimental procedure

2.1. Electron microprobe analysis

Quantitative chemical analyses were obtained with a Cameca electron microprobe (CAMECA SX 100),

operating in the wavelength-dispersion mode, with an accelerating voltage of 15 kV, a specimen current of 10 nA, and a beam diameter of approximately 10 μm ; 20 points have been analyzed.

2.2. X-ray diffraction

Several crystals of the new mineral have been examined by single crystal X-ray diffraction (XRD) using a Nonius KappaCCD diffractometer and graphite monochromated $\text{MoK}\alpha$ -radiation. Integration of intensity data has been carried out using EvalCCD (Duisenberg *et al.*, 2003). A numerical absorption correction was performed using Sadabs (Sheldrick, 2008), based on face indexing of the crystal. Intensity statistics were inconclusive regarding the presence or absence of a centre of symmetry. Table 1 shows details for the specimen, the Raman spectra of which are also presented in this article. Table 2 lists the positions of significant calculated powder diffraction maxima. Structure refinement and calculation of powder diffraction lines were performed using Jana2000 (Petricek *et al.*, 2000).

2.3. Raman spectroscopy

Raman scattering experiments were performed with a triple grating spectrometer Horiba Jobin-Yvon T64000 equipped with an Olympus BX41 microscope and a liquid-nitrogen-cooled CCD detector Symphony. The spectra were collected in back-scattering geometry with the 514.5 nm line of an Ar^+ -laser (Coherent Innova 90C Fred) and a 50 \times objective. The laser power on the sample surface was 8 mW, while the diameter of the laser spot was

Table 1. Crystal data, data collection and refinement details.

Simplified formula	$\text{Y}_{3.2}\text{Yb}_{0.8}\text{Si}_3\text{O}_8(\text{OH})_8$
Refined composition	$\text{Y}_{3.2}\text{Yb}_{0.8}\text{Si}_{2.92}\text{O}_8(\text{OH})_8$
M [g mol^{-1}]	769.02
Space group	$I\bar{4}2d$ (122)
Crystal system	tetragonal
Lattice parameters	6.947(4), 6.133(3)
a, c (\AA)	
V [\AA^3]	295.98
ρ_{calc} [g cm^{-3}]	4.31
Crystal dimensions (mm)	$0.08 \times 0.07 \times 0.07$
θ_{max} ($^\circ$)	35
hkl -range	$-11 \leq h \leq 11, -11 \leq k \leq 11, -9 \leq l \leq 8$
μ [mm^{-1}]	22.21
$T_{\text{min}}, T_{\text{max}}$	0.057, 0.16
R_{int}	0.039
$N_{\text{obs}} (I > 3\sigma(I)), N_{\text{all}}$	288, 325
$R_{\text{obs}}, R_{\text{all}}$	1.73, 2.08
Number of parameters	20
Refinement method	Full matrix least squares on F^2
Weighting scheme	$1/(\sigma^2(I) + 0.0025I^2)$
GooF	0.82
$\delta(\rho)_{\text{max}}, \delta(\rho)_{\text{min}}$ [e/\AA^3]	0.33, -0.28

Table 2. Calculated X-Ray powder diffraction data of atelisite-(Y). Strongest lines appear in bold. Only maxima with $\sum(F_{\text{hkl}})^2/(F_{\text{max}})^2 > 0.01$, $2\theta(\text{MoK}\alpha) < 30^\circ$ are shown. Observed positions and intensities have been determined by a Gandolfi type measurement of an atelisite-(Y) single crystal (n.o. = not observed). See also Fig. 6.

hkl	d_{calc} (\AA)	d_{obs} (\AA)	$\sum(F_{\text{hkl}})^2/(F_{\text{max}})^2$ (%)	I_{obs} (%)
1 0 1	4.5977	4.5805	57	45
2 0 0	3.4735	3.4645	100	100
2 1 1, 2 $\bar{1}$ 1	2.7715	2.7655	25	31
1 $\bar{1}$ 2, 1 1 2	2.6013	2.5863	73	58
2 2 0	2.4561	2.4527	20	20
2 0 2	2.2988	2.2902	7	6
3 1 0	2.1968	n.o.	2	n.o.
3 0 1	2.1664	2.1608	30	26
1 0 3	1.9612	1.9602	20	12
3 2 1, 3 $\bar{2}$ 1	1.8382	1.8407	26	23
3 1 2, 3 $\bar{1}$ 2	1.7859	1.7795	68	52
4 0 0	1.7368	1.7185	24	10
2 $\bar{1}$ 3, 2 1 3	1.7036			
4 $\bar{1}$ 1, 4 1 1	1.6247	1.6881	8	6
0 0 4	1.5333	1.5272	6	9
3 0 3	1.5326			
3 3 2, 3 $\bar{3}$ 2	1.4444	1.4154	18	14
2 0 4	1.4027	1.3736	16	17

2.5 μm . The spectral resolution was 1.9 cm^{-1} . Polarized Raman spectra were measured in $\bar{X}(ZZ)X$, $\bar{X}(YY)X$ and $\bar{X}(YZ)X$ experimental geometries (Porto's notation), where X, Y, and Z denote the crystallographic [100], [010], and [001] directions. Additional Raman scattering experiments were performed using the 441.6 nm line of a He-Cd laser (Kimmon IK Series) in order to distinguish the peaks originating from atomic vibrations (phonon modes) from possible photoluminescence peaks. The sample was fixed on the tip of a glass fibre using silicone as a glue. The spectra were collected from a flat natural surface, which exhibited homogeneous reflectivity under the illumination with white light. Additional Raman spectra taken from an empty glass fibre with attached silicone were subtracted from the sample spectrum in order to eliminate weak background signals at 490, 709, 2905 and 2964 cm^{-1} .

3. Results and discussion

3.1. Occurrence, general appearance and physical properties

The type locality, the Stetind pegmatite, Tysfjord, Nordland, Norway ($68^\circ 10' 15.20''\text{N}$ $16^\circ 33' 10.6''\text{E}$), is one of a series of quartz-microcline pegmatites of the NYF family occurring as lenticular bodies in the Tysfjord granite, a foliated, pale grey to pale red, partly recrystallized gneiss granite with annite, Fe-rich "hastingsitic hornblende", fluorite and epidote-allanite (Foslie, 1941). The granite has been dated to 1742 ± 46 Ma, and is interpreted

to originate from the partial melting of continental crust during crystallization of the older mangerites of Hamarøy and Lofoten, and later deformed during the early stages of the Caledonian orogenic cycle (Andresen & Tull, 1986). The pegmatites often contain bodies of Y-bearing fluorite with inclusions of various REE-minerals; field relationships indicate that the fluorite belongs to the latest formation in the pegmatites; see Husdal (2008) for details. The fluorite from the Stetind pegmatite forms a number of elongated to sheet-like masses along a narrow zone which can be traced for approximately ten metres in the inner parts of the quarry, and can be very rich in inclusions. The following species have been identified from this material, either as euhedral microcrystals in small voids or as grains embedded in the fluorite: allanite-(Y), allanite-(Ce), bastnäsite-(Ce), britholite-(Y) and/or fluorbritholite-(Y), calcioancylite-(Ce), calcioancylite-(Nd), fluorthalénite-(Y), hematite, hundholmenite-(Y), kainosite-(Y), keiviite-(Y), keiviite-(Yb), kozoite-(Nd), kuliokite-(Y), muscovite, quartz, rowlandite-(Y), stetindite, synchysite-(Y), thalénite-(Y), thorite, törnebohmitte-(Ce), uraninite, uranophane- β , vyuntspakhkite-(Y), xenotime-(Y), yttrialite-(Y) and zircon. Atelosite-(Y) was found in a remarkably pure fluorite, with a few scattered grains of bastnäsite-(Ce) being the only inclusions. This fluorite also differs from the normal type in being partly dissolved and altered into a white, powdery mineral and, occasionally, kainosite-(Y). The new mineral is a late, hydrothermally formed phase in dissolution cavities in this material, associated with xenotime-(Y), calcioancylite-(Nd) and La-dominant calcioancylite. Apart from a single sample found on the dumps, material containing atelosite-(Y) was restricted to a few pods, some cm across, in the quarry wall. Atelosite-(Y) occurs as well-formed, bipyramidally terminated, short-prismatic single crystals up to 0.3 mm in size, sometimes forming aggregates of randomly intergrown individuals

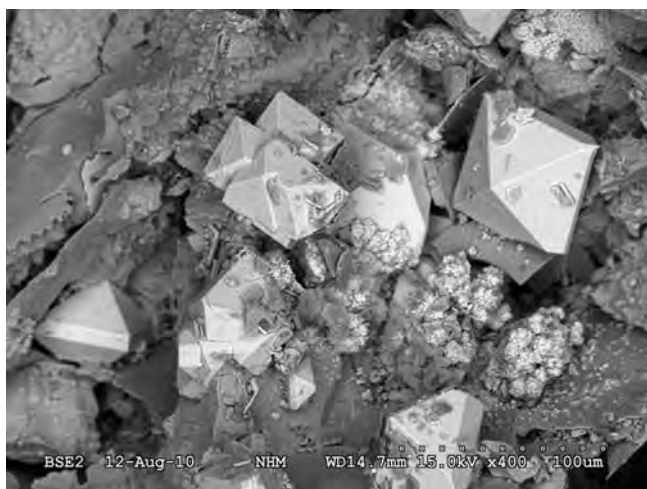


Fig. 1. Crystals of atelosite-(Y) in a dissolution cavity in yttrian fluorite from the Stetind pegmatite. SEM image by Harald Folvik, Natural History Museum, Oslo.

(Fig. 1). Displayed forms are {101}, {100}, rarely {001} and an unidentified form. The crystals are colourless to pale brown, with colourless streak and vitreous lustre. They are optically uniaxial (+) with indices of refraction $n_{\omega} = 1.727$ and $n_{\epsilon} > 1.8$ measured at 589 nm by liquid immersion ($n_{\max} = 1.8$). The calculated mean refractive index is $n_{\text{calc}} = 1.78$ using the Gladstone-Dale relation (Mandarino, 1981) with empirical formula and single crystal unit-cell data. The calculated density based on the same data is 4.26 g cm^{-3} .

3.2. Electron microprobe analysis

Microprobe analyses of atelosite exhibit low oxide totals, indirectly indicating the presence of hydrous species. The amount of available sample material was not sufficient to determine the water content quantitatively, but Raman spectra of atelosite clearly indicate the presence of hydroxyl groups. If the hydrogen content is adjusted to charge balance a formula unit containing 4 REE atoms, the measured Si and 16 anions, as expected from structure determination, the empirical composition $(\text{Y}_{3.11}\text{Yb}_{0.46}\text{Er}_{0.19}\text{Dy}_{0.11}\text{Gd}_{0.09}\text{Ho}_{0.01}\text{Tb}_{0.02})_{\Sigma 3.99}\text{Si}_{2.4}\text{O}_{16}\text{H}_{10.42}$ is obtained. The calculated water content nearly compensates the low oxide totals (Table 3) in this case. There is a clear Si deficit with respect to a hypothetical composition $(\text{REE})\text{SiO}_3(\text{OH})$. The deviation from an idealized composition $(\text{REE})_4\text{Si}_3\text{O}_8(\text{OH})_8$ can be attributed to an excess of hydrous species in combination with excess Si vacancies. This suggests the additional presence of hydrogrossular-type defects in this sample, which is clearer when the empirical formula is rearranged to become $(\text{Y}_{3.11}\text{Yb}_{0.46}\text{Er}_{0.19}\text{Dy}_{0.11}\text{Gd}_{0.09}\text{Ho}_{0.01}\text{Tb}_{0.02})_{\Sigma 3.99}(\text{Si}_{2.4}[\text{H}_4^+]_{0.605})_{\Sigma 3.01}\text{O}_8(\text{OH})_8$.

Table 3. Electron microprobe analysis results for atelosite-(Y).

Constituent	Wt %	Range	Probe standard
SiO ₂	18.73	18.20–19.21	Andradite
Y ₂ O ₃	45.67	44.04–46.61	Y ₂ O ₃
Yb ₂ O ₃	11.81	10.58–13.18	Yb ₂ O ₃
Gd ₂ O ₃	2.09	1.78–2.73	REE3
Tb ₂ O ₃	0.54	0.33–0.67	REE4
Dy ₂ O ₃	2.61	2.11–3.19	REE1
Ho ₂ O ₃	0.62	0.33–0.85	REE2
Er ₂ O ₃	4.72	4.27–5.13	REE1
H ₂ O	12.2*		
Total	98.99		

REE glass standards:

REE1 = Si : 23.27%, Al : 6.23%, Ca : 13.43%, Y : 3.97%, Pr : 3.93%, Dy : 4.02%, Er : 3.97%, O : 40.46%

REE2 = Si : 23.53%, Al : 6.3%, Ca : 13.49%, Ce : 3.93%, Eu : 3.99%, Ho : 3.92%, Tm : 4.01%, O : 40.47%

REE3 = Si : 23.56%, Al : 6.31%, Ca : 13.8%, La : 4.01%, Sm : 3.82%, Gd : 4.%, Yb : 4.03%, O : 40.43%

REE4 = Si : 24.76%, Al : 6.66%, Ca : 14.42%, Nd : 3.89%, Tb : 4.%, Lu : 3.97%, O : 41.8%. *) calculated.

3.3. Crystal structure determination

Single-crystal XRD analysis reveals that the structure of atelosite-(Y) is of the KH_2PO_4 -(KDP)-type (Frazer & Pepinsky, 1953; Nelmes, 1987), with the K-site occupied by Y and minor amounts of other REE, and with Si and vacancies replacing P. The validity of the space group symmetry $I\bar{4}2d$, as opposed to the $I4_1/amd$ symmetry of the zircon structure type, is indicated by the presence of $hk0$ diffraction maxima with odd h, k ($h+k = 2n$). The strongest such reflection is 130, measured with an $I/\sigma(I)$ -ratio of 17. The resulting structure (Table 4) is distinguished from the zircon or xenotime structure by a characteristic, alternating rotation of the SiO_4 -tetrahedra about [001]. The observed rotation of the SiO_4 tetrahedra with respect to [100] is 14° . The corresponding rotation in monazite is close to 20° . If the H-atoms are ignored, atelosite-(Y) can be interpreted as an intermediate structure between xenotime (or zircon) and monazite (Fig. 2).

The refined Si site occupancy approaches the value $3/4$ required by charge balance. However, its value depends on the model used for REE site occupancies. 20% Yb-content result at the REE-site, if the minor amounts of other lanthanide elements determined by microprobe analysis are neglected and mixed occupancy by Y and Yb is assumed. This is the model displayed in Tables 4 and 5. If the scattering power at the Y-site is calculated according to the REE content determined by microprobe analysis (77.8% Y, 11.5% Yb, 4.8% Er, 2.8% Dy and 2.3% Gd), the refined Si-site occupancy decreases to $2/3$, or 2.64 Si *pfu*. This is accompanied by mostly insignificant changes to the structural parameters shown in Tables 4 and 5, except for a slight increase in the thermal parameters of the O-atom. The Si-site occupancy refined in this model is closer to the result from microprobe analysis, but again charge compensation for the increased number of Si vacancies would require the formation of additional OH-groups coordinating these vacant sites.

Table 4. Positional parameters, equivalent isotropic displacement parameters (\AA^2) and site occupancies of atelosite with e.s.d.'s in parentheses.

Site	WP	x	y	z	U_{eq}	Occupancy
Si	4a	0	1/2	1/4	0.0076(4)	0.73(2) Si
Y	4b	0	1/2	3/4	0.0086(1)	0.80(1) Y, 0.20(1) Yb
O	16e	0.8209(3)	0.5469(3)	0.0852(4)	0.0137(5)	1.0
H	16e	0.80(2)	0.68(1)	0.15(3)	0.04(4)	0.5 H

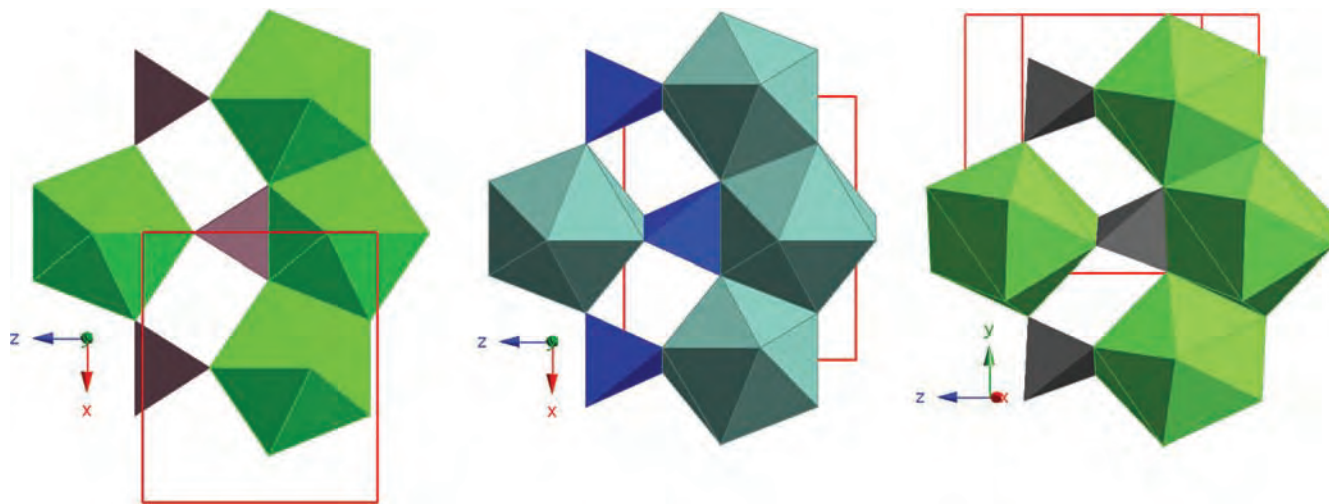


Fig. 2. Comparison of the crystal structures of xenotime (Ni *et al.*, 1995), atelosite (this work) and monazite (Ni *et al.*, 1995) in polyhedral representation from left to right. Hydrogen atoms have been omitted for atelosite.

Table 5. Anisotropic displacement parameters (\AA^2) with e.s.d.'s in parentheses.

Site	U_{11}	U_{22}	U_{33}	U_{12}	U_{13}	U_{23}
Y	0.0099(1)	0.0099(1)	0.0059(2)	0	0	0
Si	0.0081(7)	0.0081(7)	0.0067(9)	0	0	0
O	0.0093(8)	0.0198(10)	0.0122(8)	-0.0008(6)	-0.0012(6)	0.0040(7)

If the presence of the 256 forbidden $hk0$ diffraction maxima (67 with an intensity above the 3σ -level) in the unmerged data is ignored, and refinement in SG $I4_1/amd$ with the zircon structure type is attempted, the resulting figure of merit is significantly worse ($R_{\text{obs}} = 4.39$) than for the structure reported here. A very large thermal displacement parameter $U_{11} = 0.19 \text{ \AA}^2$ indicates the error of the refined oxygen position in this case.

Given its small X-ray diffraction scattering power and the expected disorder, the hydrogen position of atelсите-(Y) is not easily recognized in difference Fourier maps of the refined structure. However, hydrogen in the isostructural compound RbH_2PO_4 (RDP) has been located at $x = 0.138$, $y = 0.223$, $z = 0.125$ by neutron diffraction (Al-Karaghoulі *et al.*, 1978). Using this as a starting position, with a soft restraint of 1.04 Å imposed on the nearest neighbour O-H distance, the H-atom can be approximately located at $x = 0.20$, $y = 0.32$, $z = 0.15$ in atelсите. The resulting O-H bonds form angles of 24° with the (001) plane, and 16° with $\langle 100 \rangle$. The inclination of the split H-site trajectory with respect to (001) is approximately 20° . Literature values of this inclination for KDP or RDP (φ in Nelmes (1987)) are about 7° for the static crystal structure. It should be noted though that the soft mode for deuterated KDP (DKDP) is dominated by deuterium vibrations along a direction that is inclined to the (001) plane by 22° . This value, which might be considered as the inclination of the “dynamic” split trajectory of the corresponding site is very similar to the apparent static value in atelсите.

The resulting structure of atelсите-(Y) is shown in Fig. 3. Bond valence (bv) sums amount to 3.06 for Y/Yb, 3.94 for

Si, 1.98 for O and 0.99 for H with parameters from Brese & O’Keeffe (1991) for bond pairs Y-O, Yb-O and Si-O and from Malcherek & Schlüter (2007) for H-O. The bond valences have been calculated assuming a cutoff distance of 3.5 Å in Jana2000. The O-O distance bridged by hydrogen bonds is 2.864(3) Å, which is longer than the O-O distances of 2.572(3) and 2.720(3) Å along the edges of the SiO_4 -tetrahedron (Table 6). The primary OH-bond has a length of 1.04(9) Å (0.63 bv), as imposed by the soft distance restraint. The secondary hydrogen bond distance is 1.89(7) Å (0.14 bv). The distance to a third O-atom, located at the opposite end of the adjacent tetrahedral edge, is 2.38(14) Å (0.06 bv) (Fig. 4). This latter bond accounts for a small but significant contribution to the bond valence sum of the H-atom. The weak hydrogen-bond might explain why the primary OH-bonds and consequently the intrasite H-trajectory appear tilted against $\langle 010 \rangle$. The split

Table 6. Selected bond lengths and angles with e.s.d.’s in parentheses.

	Distance (Å)		Angle (°)
Si-O	1.636(2)		
O-O	2.572(3)	O-Si-O	103.67(11)
	2.720(3)		112.45(10)
Y-O	2.313(2)	O-Y-O	71.21(8)
	2.425(2)		92.92(7)
			75.60(7)
			82.28(7)
			64.07(7)
		Si-O-Y	147.64(12)
			96.13(9)
O-O	2.760(3)	Y-O-Y	106.51(9)
H-O	1.04(9)		
H—O	1.89(7)	O-H—O	155(12)
	2.38(14)		98(7)
	2.64(12)		108(7)
	2.78(14)		86(8)

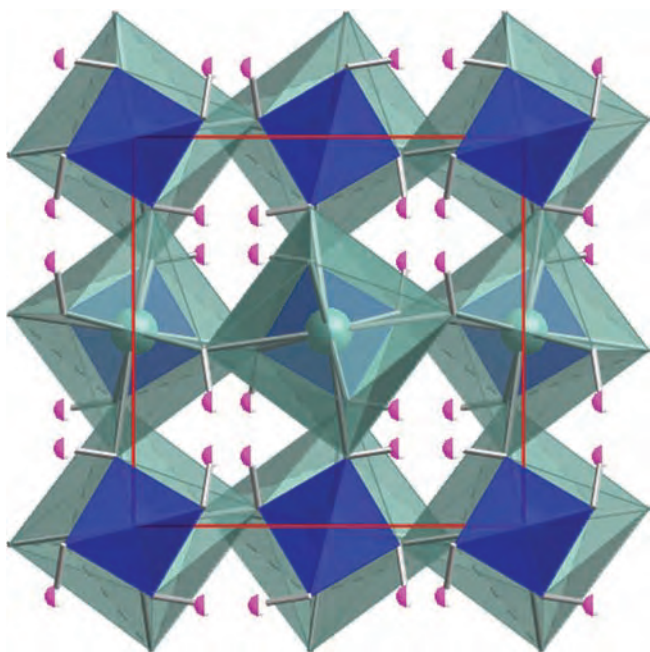


Fig. 3. Crystal structure of atelсите-(Y) in polyhedral representation, projected down [001]. One quarter of the Si-tetrahedra (blue) is vacant. Only half of the hydrogen positions (half coloured magenta) are occupied.

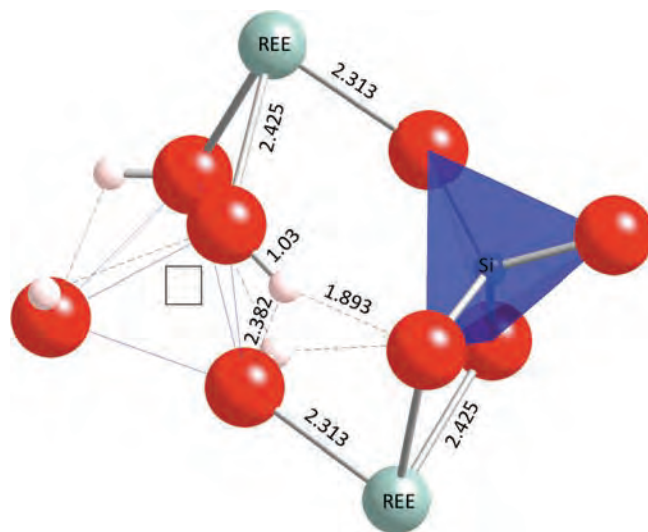


Fig. 4. Hydrogen atoms bound to the vertices of a vacant Si-tetrahedron (□). Distances are given in Å.

hydrogen positions are widely spaced at a distance of 1 Å, which is much longer than the known distance (δ in Nelmes, 1987) of about 0.35 Å in KDP or RDP. Accurate determination by neutron diffraction measurement would be required before ultimate conclusions can be drawn, but the large intrasite distance and the presence of vacancies at the tetrahedrally coordinated site suggest static distribution of H-atoms, rather than tunneling dynamics as expected for KDP (Blinic *et al.*, 1983) or other forms of dynamic disorder.

REE occur in eightfold coordination with four shorter bond distances of 2.313(2) Å and four longer distances of 2.425(2) Å. As in the zircon structure the coordination polyhedron can be interpreted as the superposition of a strongly elongated with another, strongly compressed, tetrahedron of oxygen atoms. However, contrary to the zircon structure the two distorted tetrahedra form an angle of seven degrees in atelosite-(Y). Si is tetrahedrally coordinated by four oxygen atoms at 1.636(2) Å distance. The largest thermal displacement amplitude of the O-atom occurs roughly normal to the triangle formed by one Si and two REE-cations bonding to that anion.

3.4. Raman spectroscopy

The polarized Raman spectra (Fig. 5) do show clear indication for the presence of OH groups in the structure as revealed by the broad Raman scattering centred near 3225 cm^{-1} , which originates from O-H bond stretching. The single shape of the peak, instead of a doublet typical of water (Nasdala *et al.*, 2001), as well as the absence of Raman scattering near 1600 cm^{-1} arising from H-O-H bond bending, rules out the possibility to attribute this

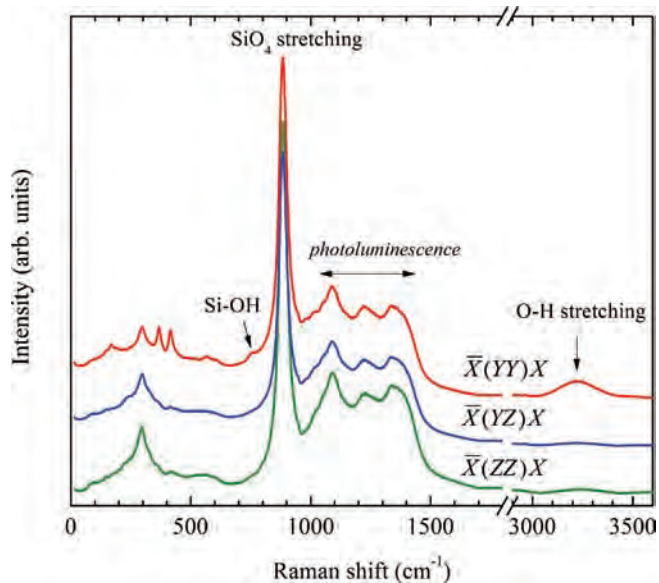


Fig. 5. Polarized Raman spectra of an atelosite-(Y) single crystal measured in $\bar{X}(YY)X$, $\bar{X}(YZ)X$, and $\bar{X}(ZZ)X$ scattering geometries (Porto's notation). Spectra have been vertically shifted for clarity. The peaks in the spectral range 1050–1450 cm^{-1} are dominated by photoluminescence.

Raman peak to H₂O molecules. The maximum is observed in $\bar{X}(YY)X$ -geometry (Fig. 5), indicating that the strongest polarizability of the O-H bond occurs within (001). This corroborates the position of hydrogen atoms obtained from the KDP structure model, in which primary OH bonds occur nearly parallel to $\langle 100 \rangle$. In terms of wavenumber and direction-dependent intensity, the Raman signal bears some resemblance to an infrared absorption band described by Talla *et al.* (2011) for xenotime, heat treated at temperatures of 1000°C and above, as well as to similar bands observed in heat treated zircon crystals (Woodhead *et al.*, 1991). The Raman scattering data do not give any evidence for differently oriented OH groups, which suggests, by analogy with OH-bearing zircon (Nasdala *et al.*, 2001), that hydrogen is not coupled to Si vacancies, *i.e.* significant hydrogrossular-type substitution is unlikely to occur in atelosite-(Y). It should be emphasized that the shape of the broad maximum resulting from the OH-stretching mode cannot be approximated by a pure Lorentzian function, but requires the use of a pseudo-Voigt function with about 70% Gaussian contribution. This indicates a high degree of static structural disorder resulting in a large variation of the O-H bond lengths. The structural disorder is likely caused by the partial occupancy and the random distribution of H and Si atoms on the corresponding crystallographic site.

According to site-symmetry group analysis (Kroumova *et al.*, 2003), there would be $6A_1 + 8B_1 + 7B_2 + 15E$ Raman active modes in atelosite-(Y), if all crystallographic sites would be totally occupied. Table 7 summarizes the Raman active modes associated with each site and their contributions to the different scattering geometries.

Due to the small size of the specimen, it was not possible to find a flat (001)-oriented surface suitable to record the $\bar{Z}(XY)Z$ Raman spectrum of atelosite-(Y). However, the other three types of polarized spectra could be collected from specimens with known orientations of the crystallographic axes that exhibited a plain surface perpendicular to $\langle 100 \rangle$. Hence, distinctive spectra should be recorded in $\bar{X}(YY)X$, $\bar{X}(YZ)X$, and $\bar{X}(ZZ)X$ scattering geometries, similar to other KDP-type materials (Percy & Samara, 1973), because modes of different symmetry type contribute to the different geometries. However, as can be seen in Fig. 5, the $\bar{X}(YZ)X$ and $\bar{X}(ZZ)X$ spectra are very similar to each other. The strong depolarization of the spectra is mainly attributed to the partial occupation of the (4a) Wyckoff position and the randomness of Si vacancies with associated

Table 7. Raman active modes associated with each site and their contributions to the different scattering geometries.

Atom	WP	$\bar{X}(YY)X, \bar{X}(ZZ)X$	$\bar{X}(YY)X$	$\bar{Z}(XY)Z$	$\bar{X}(YZ)X$
Si	4a	–	B ₁	B ₂	2E
Y/REE*	4b	–	B ₁	–	E
O	16c	3A ₁	3B ₁	3B ₂	6E
H	16c	3A ₁	3B ₁	3B ₂	6E

*The acoustic B₂ + E modes are subtracted.

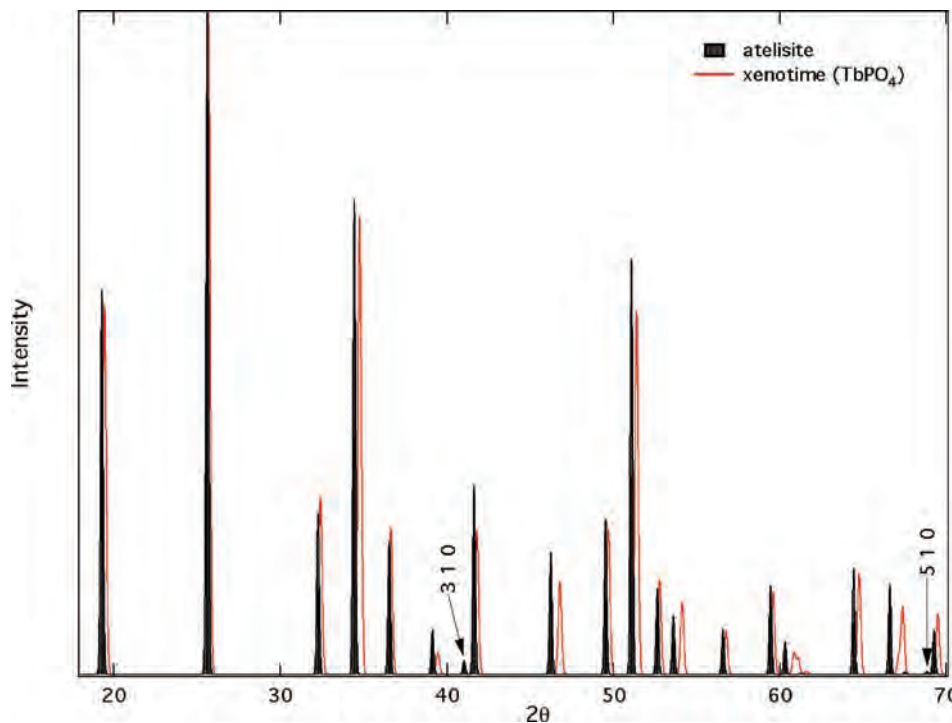


Fig. 6. Calculated powder diffraction profile ($\text{CuK}\alpha_1$ radiation) for atelinite compared to xenotime-(Tb) (Ni *et al.*, 1995) as a representative of the xenotime family with similar lattice parameters. Distinctive $hk0$ peaks of atelinite are labeled.

local structural distortions. The $\bar{X}(YY)X$ spectrum exhibits more peaks than the $\bar{X}(ZZ)X$, which can be due to B_1 -type modes or to the difference in the magnitudes of the yy and zz components of the Raman polarizability tensors of the A_1 -type modes. The latter should be particularly pronounced for modes comprising vibrations of H atoms and/or of O atoms forming O-H bonds. For example, the weak Raman peak near 755 cm^{-1} in the $\bar{X}(YY)X$ spectrum is probably related to the Si-O bond stretching of Si-OH linkages, as it only occurs in the same geometry as the main OH-stretching signal at 3225 cm^{-1} . It is observed about 100 cm^{-1} below the main SiO_4 -stretching signal at 885 cm^{-1} , in agreement with other silicates containing Si-OH linkages (Ricchiardi *et al.*, 2001). In atelinite-(Y) there are eight H atoms, three Si and one Si vacancy per unit cell. A maximum of four hydrogens may thus form hydroxyl groups with the O atoms that coordinate a vacant Si site, otherwise only bonded to adjacent REE cations (Fig. 4). The remaining four hydrogen atoms have to form hydroxyl groups with O atoms belonging to SiO_4 tetrahedra, thus constituting the Si-OH linkages evidenced by the weak signal at 755 cm^{-1} .

4. Conclusions

In terms of crystal structure, atelinite-(Y) is closely related to the nominally anhydrous minerals zircon and xenotime. While its crystal structure is similar to KDP, it differs from KDP in its incompletely filled tetrahedral site. Raman spectroscopy confirms the KDP-type structure model for atelinite, as OH-bonds are predominantly oriented normal

to $[001]$. With respect to zircon, two substitution schemes can be identified, that, mutually applied, generate the atelinite-(Y) composition: $4\text{Zr}^{4+} = 4\text{Y}^{3+} + 4\text{H}^+$ and $4\text{Si}^{4+} = 3\text{Si}^{4+} + 4\text{H}^+$. As both substitution schemes have been postulated for hydrogen incorporation into zircon, the structure of atelinite might be relevant to the local structure of zircon and xenotime containing minor amounts of hydrous species. Due to its similarity to xenotime, both in appearance and by powder X-ray diffraction (Fig. 6), atelinite might be more common than its very recent discovery would suggest. Further study of the new mineral with respect to its mixing behaviour, hydrogen bonding and possible ferroelectric properties is going to require synthetic material though.

Acknowledgements: The authors would like to thank S. Heidrich for conducting the microprobe analysis, P. Stutz for the polished sections of the new mineral and P. Bøe for assistance during the discovery of the new mineral.

References

- Al-Karaghoul, A.R., Abdul-Wahab, B., Ajaj, E., Sequeira, A. (1978): A precision neutron diffraction study of tetragonal RbH_2PO_4 . *Acta Cryst.*, **B34**, 1040–1042.
- Andresen, A. & Tull, J.F. (1986): Age and tectonic setting of the Tysfjord gneiss granite, Etfjord, North Norway. *Norsk. Geol. Tidsskr.*, **66**, 69–80.

- Blinic, R., Žekš, B., Nelmes, R.J. (1983): Proton tunneling in KH_2PO_4 . *Phase Transitions*, **3**, 293–308.
- Brese, N.E. & O'Keefe, M. (1991): Bond-valence parameters for solids. *Acta Cryst.*, **B47**, 192–197.
- Duisenberg, A.J.M., Kroon-Batenburg, L.M.J., Schreurs, A.M.M. (2003): An intensity evaluation method: EVAL-14. *J. Appl. Cryst.*, **36**, 220–229.
- Foslie, S. (1941): Tysfjords geologi. Beskrivelse til det geologiske gradteigskart Tysfjord. *Norges Geologiske Undersøkelse*, **149**, 298 pp.
- Frazer, B.C. & Pepinsky, R. (1953): X-ray analysis of the ferroelectric transition in KH_2PO_4 . *Acta Cryst.*, **6**, 273–285.
- Husdal, T.A. (2008): The minerals of the pegmatites within the Tysfjord granite, Northern Norway. Kongsberg Mineralsymposium 2008. Bergverksmuseum, **38**, 5–28.
- Kroumova, E., Aroyo, M.I., Perez-Mato, J.M., Kirov, A., Capillas, C., Ivantchev, S., Wondratschek, H. (2003): Bilbao crystallographic server: useful databases and tools for phase-transition studies. *Phase Transitions*, **76**, 155–170.
- Malcherek, T. & Schlüter, J. (2007): $\text{Cu}_3\text{MgCl}_2(\text{OH})_6$ and the bond valence parameters of the OH—Cl bond. *Acta Cryst.*, **B63**, 157–160.
- Mandarino, J.A. (1981): The Gladstone-Dale relationship: part IV. The compatibility concept and its application. *Can. Mineral.*, **19**, 441–450.
- Nasdala, L., Beran, A., Libowitzky, E., Wolf, D. (2001): The incorporation of hydroxyl groups and molecular water in natural zircon (ZrSiO_4). *Am. J. Sci.*, **301**, 831–857.
- Nelmes, R.J. (1987): Structural studies of KDP and the KDP-type transition by neutron and X-ray diffraction: 1970–1985. *Ferroelectrics*, **71**, 87–123.
- Ni, Y., Hughes, J.M., Mariano, A.N. (1995): Crystal chemistry of the monazite and xenotime structures. *Am. Mineral.*, **80**, 21–26.
- Percy, P.S. & Samara, G.A. (1973): Pressure and temperature dependences of the dielectric properties and raman spectra of RbH_2PO_4 . *Phys. Rev. B*, **8**, 2033–2048.
- Pekov, I.V., Zubkova, N.V., Chukanov, N.V., Husdal, T.A., Zadov, A.E., Pushcharovsky, D.Y. (2011): Fluorbritholite-(Y), $(\text{Y,Ca,Ln})_5[(\text{Si,P})\text{O}_4]_3\text{F}$, a new mineral of the britholite group. *N. Jb. Miner. Abh.*, **188**, 191–197.
- Petricek, V., Dusek, M., Palatinus, L. (2000): Jana2000. The crystallographic computing system. Institute of Physics, Praha, Czech Republic.
- Raade, G., Johnsen, O., Erambert, M., Petersen, O.V. (2007): Hundholmenite-(Y) from Norway - A new mineral species in the vicanite group: descriptive data and crystal structure. *Mineral. Mag.*, **71**, 179–192.
- Ricchiardi, G., Damin, A., Bordiga, S., Lamberti, C., Spano, G., Rivetti, F., Zecchina, A. (2001): Vibrational structure of titanium silicate catalysts. A spectroscopic and theoretical study. *J. Am. Ceram. Soc.*, **123**, 11409–11419.
- Schlüter, J., Malcherek, T., Husdal, T.A. (2009): The new mineral stetindite, CeSiO_4 , a cerium end-member of the zircon group. *N. Jb. Miner. Abh.*, **186**, 195–200.
- Sheldrick, G.M. (2008): Sadabs, v. 2008/1. Program for empirical absorption correction of area detector data. University of Göttingen, Göttingen, Germany.
- Talla, D., Beran, A., Škoda, R., Losos, Z. (2011): On the presence of OH defects in the zircon-type phosphate mineral xenotime, $(\text{Y,REE})\text{PO}_4$. *Am. Mineral.*, **96**, 1799–1808.
- Trail, D., Thomas, J.B., Watson, E.B. (2011): The incorporation of hydroxyl into zircon. *Am. Mineral.*, **96**, 60–67.
- Vogt, T. (1911): Vorläufige Mitteilung über Yttrofluorit, eine neue Mineralspezies aus dem nördlichen Norwegen. *Centralblatt für Mineralogie, Geologie und Paläontologie*, **1911**, 373–377.
- Woodhead, J.A., Rossman, G.R., Thomas, A.P. (1991): Hydrous species in zircon. *Am. Mineral.*, **76**, 1533–1546.

Received 15 March 2012

Modified version received 13 April 2012

Accepted 29 May 2012